EBNA1-targeted probe for the imaging and growth inhibition of tumours associated with the Epstein–Barr virus

Lijun Jiang[1], Rongfeng Lan[1], Tao Huang[2], Chi-Fai Chan[3], Hongguang Li[1], Sam Lear[4], Jingyi Zong[4], Wing-Yan Wong[3], Magnolia Muk-Lan Lee[3], Brandon Dow Chan[3], Wai-Lun Chan[1], Wai-Sum Lo[3], Nai-Ki Mak[5,6], Maria Li Lung[6,7], Hong Lok Lung[5,6], Sai Wah Tsao[6,8], Graham S. Taylor[9], Zhao-Xiang Bian[2], William C. S. Tai[3], Ga-Lai Law[3]*, Wing-Tak Wong[3]*, Steven L. Cobb[4]* and Ka-Leung Wong[1]*

[1]Department of Chemistry, Hong Kong Baptist University, Kowloon Tong, Hong Kong SAR, China.

[2]Clinical Division, School of Chinese Medicine, Hong Kong Baptist University, Kowloon Tong, Hong Kong SAR, China.

[3]State Key Laboratory of Chiroscience, Department of Applied Biology and Chemical Technology, Hong Kong Polytechnic University, Hung Hum, Hong Kong SAR, China.

[4]Department of Chemistry, Durham University, Durham DH1 3LE, UK.

[5]Department of Biology, Hong Kong Baptist University.

[6]Centre for Nasopharyngeal Carcinoma Research, University of Hong Kong, Hong Kong SAR, China.

[7]Department of Clinical Oncology University of Hong Kong , Hong Kong SAR, China.

[8]School of Biomedical Sciences University of Hong Kong, Hong Kong SAR, China.

[9]School of Cancer Sciences, University of Birmingham, Vincent Drive, Birmingham B15 2TT, UK.

*e-mail: nkmak@hkbu.edu.hk; ga-lai.law@polyu.edu.hk; bcwtwong@polyu.edu.hk; s.l.cobb@dur.ac.uk; klwong@hkbu.edu.hk

Epstein–Barr nuclear antigen 1 (EBNA1), a dimeric oncoprotein of the Epstein–Barr virus (EBV), is essential for both viral- genome maintenance and the survival of infected cells. Despite EBNA1's potential as a therapeutic target, tools for the direct monitoring of EBNA1 *in vitro* and *in vivo* are lacking. Here, we show that a peptide-based inhibitor that luminesces when bound to EBNA1 inside the nucleus of EBV$^+$ cells can regulate EBNA1 homodimer formation and selectively inhibit the growth of EBV$^+$ tumours of nasopharyngeal carcinoma cells (C666-1 and NPC43) and Burkitt's lymphoma Raji cells. We also show that the peptide-based probe leads to 93% growth inhibition of EBV$^+$ tumours in mice. Our findings support the hypothesis that selec- tive inhibition of EBNA1 dimerization can be used to afford better EBV-related cancer differentiation, and highlight the potential application of the probe as a new generation of biotracers for investigating the fundamental biological function of EBNA1 and for exploring its application as a therapeutic target.

The Epstein – Barr virus (EBV) is a ubiquitous human herpes virus that causes both infectious mononucleosis and lymphoproliferative diseases[1,2], but the virus is well controlled by the immune system once it establishes latent infection in human hosts[3,4]. Epstein – Barr nuclear antigen 1 (EBNA1) is the only oncoprotein expressed in all EBV-positive tumours and it plays critical roles in the maintenance, replication and transcription of the EBV genome. Furthermore, it can influence cellular gene transcription, which is fundamental to the development of EBV-related tumours[5]. Given these key biological functions, EBNA1 has become an attractive target for therapeutic intervention[6,7]. Considering that homodimerization of EBNA1 is essential for EBNA1 to function, inhibitors that can specifically prevent the dimerization process offer a novel avenue by which

to target and kill EBV-positive cells[8,9]. Several EBNA1 inhibitors have been reported to efficiently block EBNA1 homodimerization, including the small molecule, EiK1, and a short EBNA1-derived peptide, P85. EiK1 was identified via high-throughput screening, and is capable of targeting the dimeric interface of EBNA1 (residues 459 – 607). P85, which contains a short EBNA1-derived β3 sheet (residues 560 – 566), also targets this region (residues 560 – 574)[8]. However, most of the EBNA1-targeting compounds that have been reported to date cannot be easily imaged (*in vitro*) and they have low bioavailability. Both the aforementioned issues present major challenges to the field and hamper the further development of EBNA1-targeting therapeutics. To overcome the non-fluorescent nature and poor water solubility of the previously reported EBNA1 inhibitors, we recently designed a novel hybrid system, which contained a charged, water-soluble chromophore and an EBNA1-specific peptide. The charged, water-soluble chromophore – peptide bioconjugate, JLP_2, enabled for the first time both simultaneous specific imaging and inhibition of EBNA1 *in vitro*[9]. However, JLP_2 lacked specific subcellular localization and displayed no responsive binding, which limited its further development as a tool for cellular imaging, and as a potential selective therapeutic agent for the treatment of EBV cancers.

It is also worth noting that EBNA1 is primarily localized in the nucleus of EBV-positive cells[10], and EBNA1 acts as a bridge between mitotic chromosomes and origin of replication (*oriP*) plasmids[11]. One factor that has limited the success of cancer therapies is the challenge of specifically targeting a desired cell type[12]. Despite the key role and the specific localization of EBNA1, a direct and sensi- tive system for visualizing EBNA1 in the nucleus and monitoring its effect on EBNA1 homodimerization is not currently available. To address this problem, we reasoned that valuable new insights and selective tumour inhibition both *in vitro* and *in vivo* could be gained if a nucleus-penetrating EBNA1-specific dual-probe could be developed. The development of responsive nucleus-specific bioprobes for *in vitro* microscopic studies of EBNA1 and selective inhibition of EBV-positive tumours has not yet been explored in detail. The work reported here offers a strategy for responsive-emission imaging in EBV-positive cells and provides highly selective and efficient in vitro/vivo cytotoxicity.

The rational design (Fig. 1a) of the dual-function peptide- conjugate probes, L_2P_2, L_2P_3 and L_2P_4, was achieved using docking and molecular dynamics (MD) simulations and their synthesis is outlined in Supplementary Fig. 1. The characterization (including ^1H NMR, ^{13}C NMR and mass spectrometry) of all intermediates and final products were performed as shown in Supplementary Figs 37 – 48. The peptide conjugates were purified via high-performance liquid chromatography; the purification and characterization procedures are provided in Supplementary Figs 2 – 6, and the solvent gradients are given in Supplementary Tables 1 and 2. The L_2P_4 probe interacted strongly with wild-type EBNA1 (WT-EBNA1) as confirmed by an 8.8-fold increase in its emission intensity. L_2P_4 responded significantly on binding with WT-EBNA1, and the responsive signal was found to be induced by the intermolecular charge transfer (ICT) mechanism (Fig. 2). Simultaneous imaging and growth control of EBV-positive tumours has been achieved by our rationally designed dual-function fluorescent probes through selective interference with EBNA1 homodimerization. L_2P_4 was highly cytotoxic for EBV-positive cells (half-maximum inhibitory concentration, $IC_{50} \approx 15$ μM), but minimally so for EBV-negative cells, even at high doses (50 μM). Furthermore, L_2P_4 exhibited strong *in vivo* toxicity against EBV-positive tumours (intra-tumour injection of 4 μg resulted in 92.8% growth inhibition).

Both the *in vitro* and *in vivo* studies described here demonstrated the effectiveness of L_2P_4 as a dual EBV tumour-selective cancer targeting agent and responsive imaging probe. Given these findings, we envisage that L_2P_4 represents an efficient tool to delineate the processes that govern EBNA1 in the nucleus. In the longer term, this new level of understanding will provide exciting opportunities for the treatment of EBV-associated tumours, such as Hodgkin lymphoma, nasopharyngeal carcinoma

and a sub-group of EBV- associated stomach cancers.

Results

Rational design and MD simulations of probes. The X-ray crystal structure of EBNA1's DNA-binding domain (protein database ID, 1B3T; chain A; residue 461 to 607) is an α/β mixed fold comprised of four alpha-helix and four beta-sheet motifs that are linked by several loops (Fig. 1b and Supplementary Fig. 7)[13]. Different structural motifs contribute to its distinct functional regions: the beta sheets, β1 – β4, drive formation of the dimer via hydrophobic packing; the alpha helices, α1 and α2, interact with DNA via electrostatic interactions, while α3 and α4 stabilize the beta sheets; the positively charged loop 1 mediates DNA binding; and the flexible loop 5 is involved in the dimerization[14].

The putative structure of the EBNA1 DNA-binding domain monomer was generated from the X-ray crystal structure of its homodimer, and it was used to perform 200 ns all-atom explicit-sol- vent MD simulations in AMBER 14 (ref. [15]). The putative structure exhibited good stability and maintained the original conformation during the simulation, except for the highly dynamic loops 1 and 5, which make no contribution to the homodimerization of EBNA1 (Supplementary Fig. 8a,b). Moreover, the four beta sheets that com- prise the dimeric interface were also found to exhibit good stability (Supplementary Fig. 8c). The accessibility of the dimeric interface in the putative structure was examined, and the results suggest that the key residues (Y_{561}, M_{563} and F_{565}) on the dimeric interface[8] could be accessed by extrinsic probes (Supplementary Fig. 8d). After checking the stability and accessibility of this putative structure, a representative conformation was selected and a docking study was carried out to identify the best docked poses for each ligand – EBNA1 complex (Supplementary Fig. 8e,f). All docked poses were then ranked using a scoring function to choose the final poses for each complex. It was found that most selected poses shared some similarities; for example, the interaction of the key residues in EBNA1 with a YFMVF motif appeared in all complexes (Supplementary Fig. 9). Furthermore, unexpected salt-bridging was found between the positively charged tetrapeptide RrRK and the aspartate-rich tail in EBNA1, suggesting a secondary role for this nuclear localization sequence.

To better characterize the ligand – EBNA1 complex and calculate the binding energy, 200 ns MD simulations were performed using the selected docked poses. The AMBER (assisted model building with energy refinement) types of the non-standard residues were parameterized (Supplementary Fig. 10) and the missing force field parameters were defined (Supplementary Table 3) before running the MD simulations. All complexes were found to be stable after 50 ns, but it was difficult to find a binding pattern that was con- served between them, although they shared the YFMVF motif. This was due to the effect of the salt-bridge interaction, which appeared only in the ligands containing the RrRK tetrapeptide. Despite this, the main interactions suggested by the MD simulations for each complex were similar (clear hydrophobic contacts and salt-bridging; Supplementary Fig. 17). The hydrophobic interactions occurred between the ligands and the key residues on the dimeric interface, while the salt bridging occurred between the RrRK motif and several residues in the aspartate-rich tail in EBNA1 (D_{602}, D_{601} and D_{605}). In particular, D_{602} demonstrated the strongest salt-bridge interaction and D_{605} showed the weakest (Supplementary Figs 11 – 16). Taken together, the MD simulations suggest two major interaction types, which facilitate the binding of the designed probes to EBNA1. They also demonstrated a secondary role for the RrRK sequence beyond nuclear localization (Fig. 1b).

The binding free energy for all complexes was calculated via the molecular mechanics Poisson – Boltzmann surface area (MMPBSA) method. The calculated generalized Born (GB) and Poisson – Boltzmann (PB) values took the same order, $L_2P_4 > L_2P_3 > L_2P_2$ (Fig. 1c and Supplementary Table 4), indicating that L_2P_4 would probably have the strongest binding interaction with EBNA1.

It should be noted that the X-ray crystal structure of the EBNA1 monomer has not yet been solved and that the use of a putative one could result in errors in the numerical data generated via MD simulations. In addition, the rigid protein model used in the MOE- Dock 2012.10 (Chemical Computing Group) approach, the implicit solvent environment in the docking experiment and an untrained scoring function for the protein – peptide case, may also introduce errors into the determination of the initial structures and thus into the subsequent MD simulations. Owing to the potential for such errors, the results of the MD simulations for the proposed protein – ligand complexes should be viewed as indicative rather than definitive values. Nonetheless, the overall binding trends predicted by the simulations were clearly consistent with the experimental results; for example, L_2P_4 was shown to have the strongest binding interaction with WT-EBNA1.

Responsive emission of L_2P_4 with EBNA1.

The stability of the probes, assessed by monitoring their emission spectra at 37 °C for 24 h, was confirmed in the simulated extracellular anion mixture (PBS buffer) (Supplementary Fig. 18). As discussed in the previous section, the MD simulations and free energy calculations predicted that L_2P_4 would have the strongest interaction with WT-EBNA1, and thus it potentially offered the best option by which to prevent the homodimerization of EBNA1 and ultimately inhibit the growth of EBV-positive tumours. To assess the actual binding affinity of L_2P_4 to WT-EBNA1, a luminescence titration experiment was carried out in PBS buffer. The results aligned well with the calculated data. For example, L_2P_4 was found to have the strongest emission response on addition of 4 μM of WT-EBNA1 (Fig. 2a – c and Supplementary Fig. 21), an 8.8-fold emission enhancement and a 25 nm blue- shift. The quantum yields for L_2P_4 with and without the addition of WT-EBNA1 were calculated as shown in Supplementary Figs 19 and 20. Under the same conditions, a 4.7-fold increase in intensity was observed for L2P3, and no intensity change was observed for L2P2 (Supplementary Fig. 21). The affinity of a probe for a protein can be quantified via the binding constant and the binding ratio. The binding constant (log K_{assoc}) of the three probes to WT-EBNA1 was calculated (Supplementary Fig. 21). The logarithm of the flu- orescence ratio exhibited a linear relationship with respect to the protein concentration. The value of log K_{assoc} was calculated to be 5.50 and 6.82 for L2P3 and L2P4 respectively, and both of the bind- ing ratios were found to be 1:1. On account of its greater binding strength, we further investigated the binding selectivity of L2P4 for WT-EBNA1 in the presence of various proteins (Fig. 2c) and bio- logically relevant metal ions and small molecules, such as Zn2+ and citrate (Supplementary Figs 22 and 23). The proteins analysed in the selectivity assay included four EBNA1 mutant proteins and bovine serum albumin (BSA). EBNA1 mutant proteins were prepared by mutation of YFMVF to FFAVA (yielding EBNA1-3A) or via conservative point mutation of Y_{561}, M_{563} and F_{565} to A (yielding EBNA1- $Y_{561}A$, EBNA1-$M_{563}A$ and EBNA1-$F_{565}A$). The selectivity of L_2P_4 for each protein was investigated by recording changes in its emission. A relatively small emission enhancement was observed (Fig. 2c) on addition of the four mutant EBNA1 proteins and BSA, suggesting that the binding of L_2P_4 was weaker for these proteins than for WT-EBNA1 (log K_{assoc} values for EBNA1-$Y_{561}A$, EBNA1-$M_{563}A$, EBNA1-F565A and EBNA1-3A were 5.1, 3.6, 4.3 and 3.9, respectively; for BSA, log Kassoc was 4.7).

It is well established that when an environment-sensitive fluorophore is conjugated to peptides with specific targeting, subsequent protein binding will increase the emission intensity and a strong blueshift will occur due to the marked change in excited-state dipole moments. It is well known now that the dual fluorescence of 4-(N,N-dimethylamino)benzonitrile arises due to an emission from the local excited state and an ‘anomalous’ redshifted emission from the ICT state[16 – 18]. Among the numerous analogues of this molecule reported to date, pyridine derivatives have been a focus of particular interest, especially in the determination of cell microviscosity[19]. With this in mind, we proposed that a fluorescent probe consisting of an ICT-state pyridine-derivative fluorophore and a nucleus-permeable EBNA1-specific peptide, generating ICT-based emission after bind- ing EBNA1,

could prevent the homodimerization of EBNA1 while also enabling nucleus-level imaging of EBV-positive cells.

The absorption spectrum of L_2P_4 was measured in various sol- vents (Supplementary Fig. 24). The spectra showed two absorption bands at 274 nm and ~500 nm, which corresponded to the transition from ground state to local excited and ICT states, respectively[18,20]. The maximum absorption band was slightly redshifted in polar solvents. L_2P_4 demonstrated dual fluorescence on excitation: a weak but higher energy emission at 560 nm arising from the local excited state and a strong emission at ~625 nm from the ICT state were both observed (Fig. 2a,d,e). The fluorescence emission of the local excited band was solvent-independent, while the ICT band exhibited a marked dependence on solvent polarity, progressively blueshifted with decreasing solvent polarity (Fig. 2e). Additionally, the emission decay of L_2P_4 was measured as shown in Fig. 2f, upper (λ_{ex} = 475 nm; monitored at 625 nm) and Supplementary Fig. 26, and the emission lifetime of L_2P_4 in different solvents is shown in Supplementary Table 5. The observed shorter lifetime (~0.5 ns) corresponded to the local excited emission, and the ICT band exhibited a longer lifetime (3.8 ns).

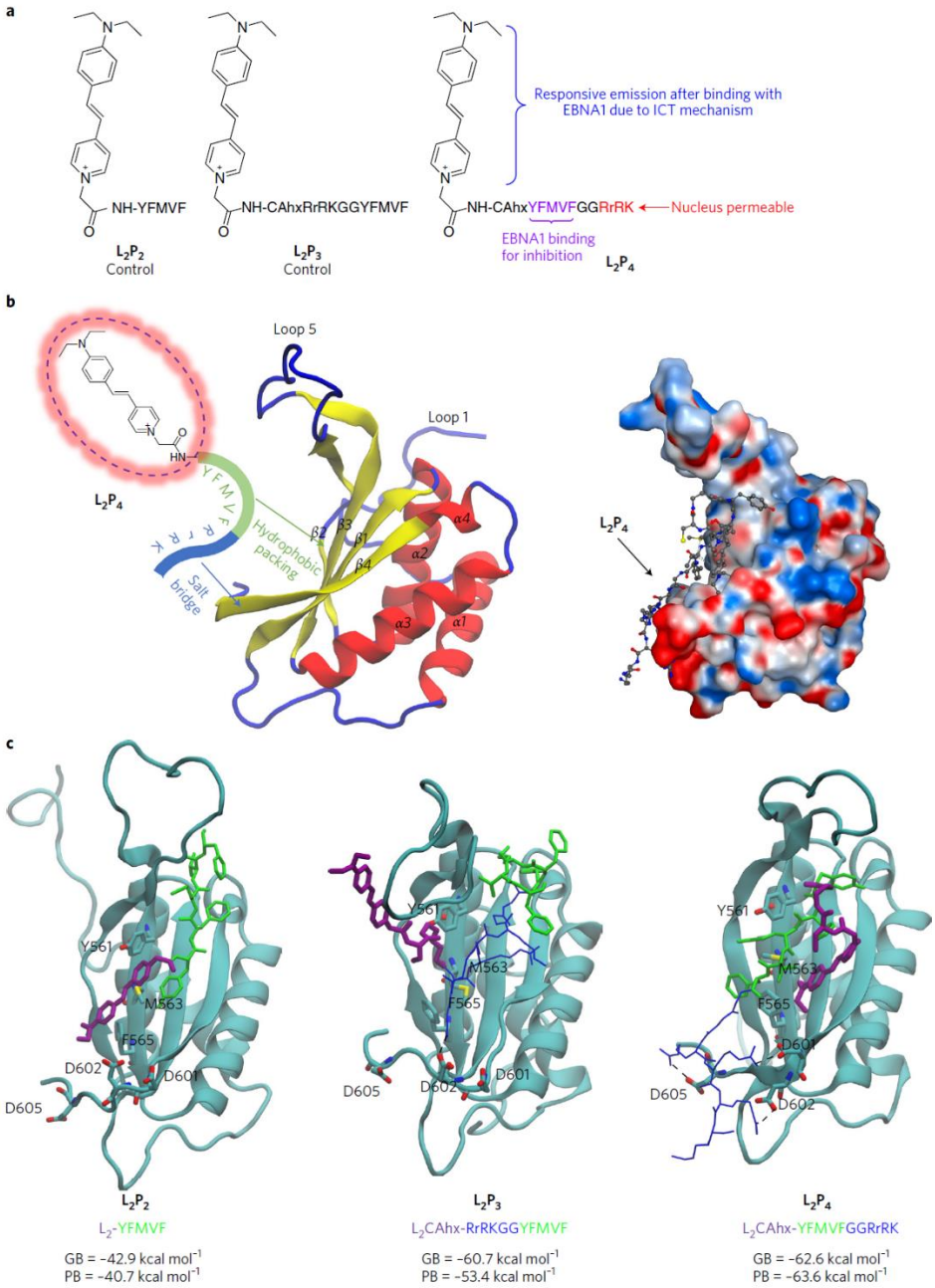

Figure 1 | Rational design of probes and MD simulations of their binding to EBNA1. **a**, The chemical structures of the designed probes (L_2P_2, L_2P_3 and L_2P_4). P_2 is a peptide derived from β4 of EBNA1 and it is EBNA1-specific. The P_3 and P_4 peptides are EBNA1-specific and nucleus-penetrating (due to addition of the RrRK motif in the middle (P_3) or at the C-terminus (P_4) of the sequence). The fluorescent group is always located at the N-terminus of P_2, P_3 and P_4. **b**, Interactions between L_2P_4 and the putative monomer structure of the EBNA1 DNA-binding domain, as suggested by MD simulations; EBNA1 is rendered as ribbons (left) and as an electrostatic surface (right). The putative structure was generated via the isolation of the X-ray crystal structure of the EBNA1–DNA complex (protein database ID: 1B3T). It is suggested that the designed probes bind to the EBNA1 dimeric interface primarily via hydrophobic interactions with the YFMVF motif, and that such interactions can be enhanced by further electrostatic interactions with the RrRK motif. The dashed oval denotes the red emissive ligand (L_2). **c**, Representative conformations of the designed probes and EBNA1 in the MD simulation. The calculated generalized Born (GB) and Poisson–Boltzmann (PB) values represented the binding free energy between the designed probes and EBNA1.

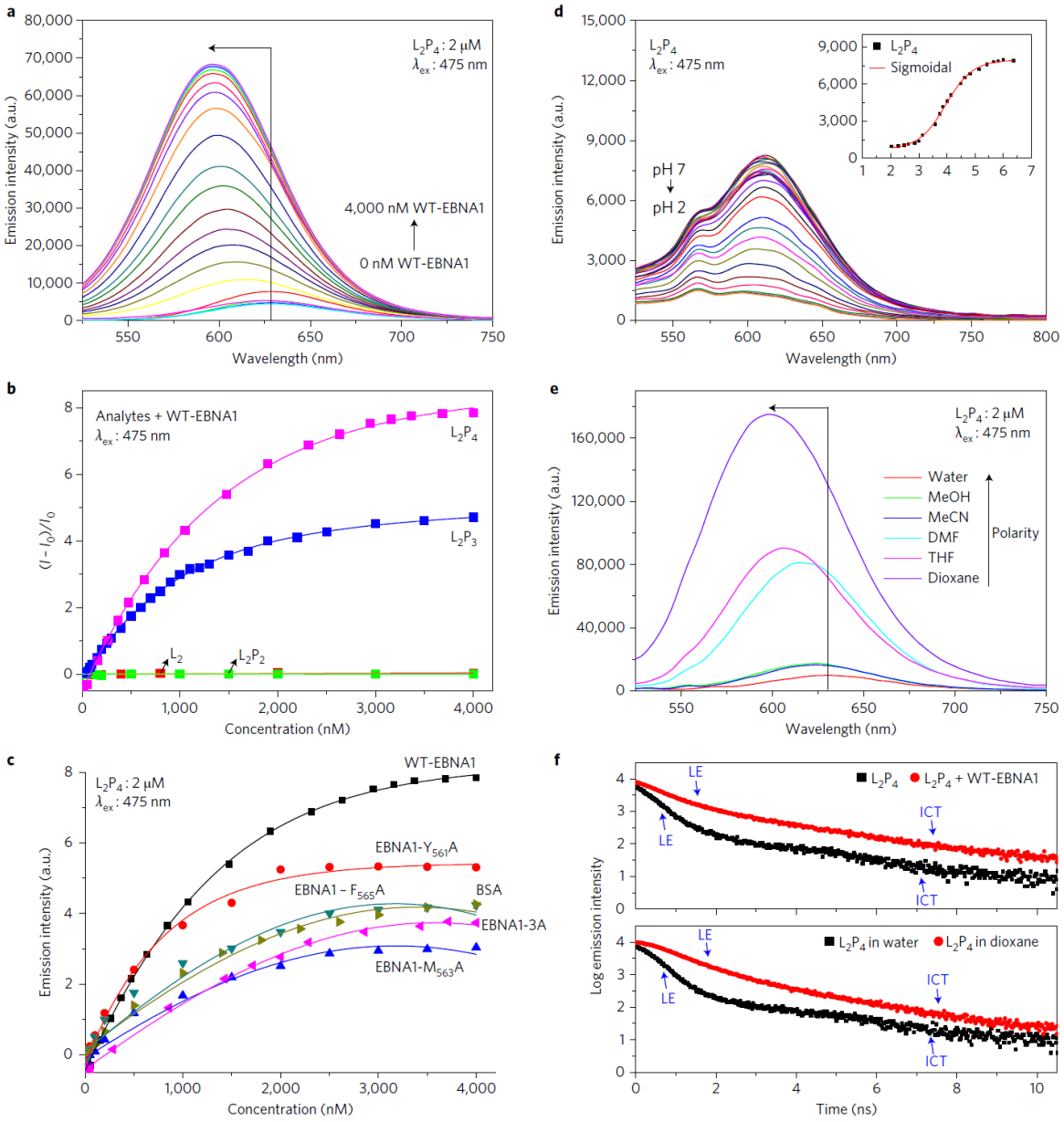

Figure 2 | Selectivity and emission of L_2P_4 on addition of EBNA1. **a**, The emission spectra of L_2P_4 showing 8.8-fold intensity increase and 25 nm blueshift in response to the addition of WT-EBNA1 (indicated by the right-angled arrow). λ_{ex}, excitation wavelength. **b**, Change in emission intensity of L_2, L_2P_2,L_2P_3 and L_2P_4 on addition of WT-EBNA1. **c**, Selectivity of L_2P_4 for various proteins; represented by emission intensity in arbitrary units (a.u.). **d**, Emission spectra of L_2P_4 for various buffer pH values; used to confirm the ICT state and determine the pK_a value (data for L_2P_3 are shown in Supplementary Fig. 25). The emission band gradually decreased as the pH was lowered from 7 to 2, which is consistent with the characteristics of ICT emission. ICT emission decreases at lower pH because the nitrogen atoms become protonated, thereby making their lone pairs unavailable for generation of an ICT excited state. **e**, L_2P_4 emission spectra from solvatochromism experiments showing the effect of decreasing the solvent polarity. **f**, Emission lifetime (decay) of L_2P_4 on binding WT-EBNA1 (upper) and solvatochromism (lower) with increasing solvent polarity (λ_{ex} = 475 nm). Comparatively large local excited (LE) emission decays and correspondingly smaller ICT decays were found in less polar solvents, indicating a smaller dipole moment and consequently an upshift of the ICT state. Additionally, the emission lifetime of L_2P_4 on binding WT-EBNA1 was found to be similar to that in polar solvents.

In vitro nuclear imaging of L_2P_4.

To evaluate whether selective nuclear localization was achieved, EBV-positive (C666-1 and NPC43) and EBV-negative (CNE2 and HeLa) cell lines were imaged *in vitro* for L_2P_2, L_2P_3 and L_2P_4 (Fig. 3). C666-1 is a nasopharyngeal carcinoma (NPC) cell line, NPC43 is a newly derived NPC cell line, which was established from the surgically resected NPC tissue of a male patient (64 years old with stage III recurrent NPC), CNE2 is an NPC cell line, and HeLa is a human cervical carcinoma cell line. As previously discussed, we incorporated the nuclear localization sequence, RrRK, into P_3 and P_4 to enhance their nucleus permeability[21,22]. The cellular uptake and localization of the three probes was evaluated independently using confocal imaging and flow cytometry (Fig. 3 and Supplementary Figs 28, 29 and 30). From these experiments, L_2P_4 was found to exhibit the highest cellular uptake in both HeLa and C666-1 cells (Supplementary Fig. 28). Owing to the contribution of RrRK, nuclear localization of L_2P_3 and L_2P_4 was observed in the EBV-positive cells (C666-1 and NPC43), whereas L_2P_2 was only found in the cytoplasm, suggesting that L_2P_3 and L_2P_4 localize in the nuclei of the EBV-positive cells. Additionally, two videos of L_2P_4 (10 μM) in HeLa and C666-1 cells were recorded (Supplementary Videos 1 and 2; one image per minute for the first hour of probe treatment). The video shows a dynamic and intuitive visualization of the selective nuclear localization of L_2P_4 in EBV-positive cells.

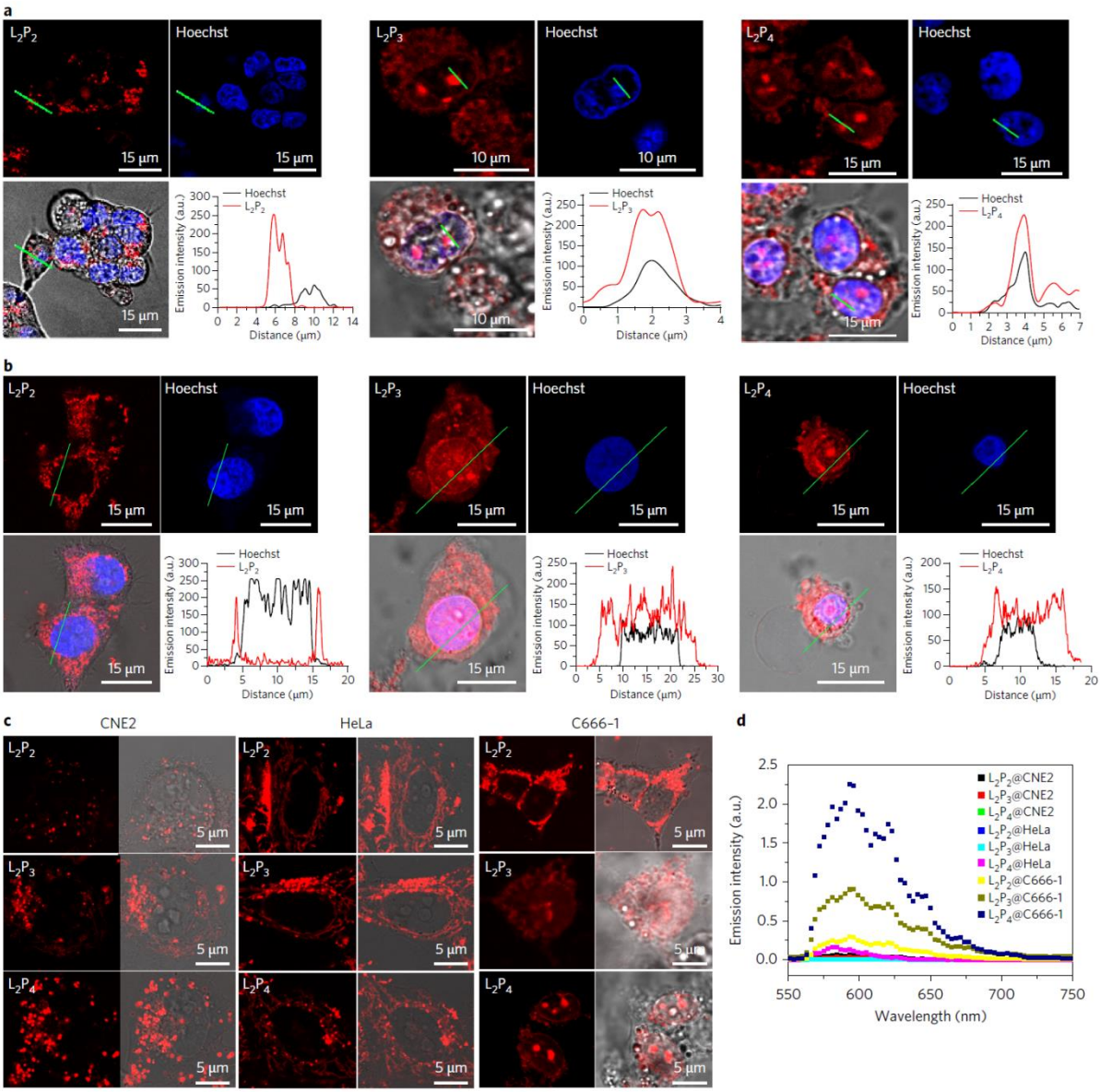

Figure 3 | *In vitro* imaging of probes in EBV-positive and EBV-negative cells. **a**,**b**, *In vitro* confocal microscopy of the L_2P_2, L_2P_3 and L_2P_4 probes in EBV- positive nasopharyngeal carcinoma cells, C666-1 (**a**) and NPC43 (**b**). λ_{ex} = 488 nm; emission wavelength, λ_{em} = 500–650 nm; filter, BP500. C666-1 and NPC43 cells were treated with L_2P_2, L_2P_3 or L_2P_4 (10 μM) for 6 h, and then co-stained with the nuclear dye Hoechst 33342 (1 nM) for 1 h. Profiles of the emission intensity of the probes and Hoechst 33342 were plotted along the green line. For the L_2P_4 found in the nucleus (by lambda scan), the shape and location of the emission band was similar to the data obtained for the solution under the same excitation. **c**, *In vitro* confocal imaging of L_2P_2, L_2P_3 and L_2P_4 in EBV-negative (CNE2 and HeLa) and EBV-positive (C666-1) cells. The emission of L_2P_4 was found to be selective for EBV-positive cells over EBV-negative cells. **d**, *In vitro* emission spectra (from confocal microscopy) of L_2P_2, L_2P_3 and L_2P_4 in the nucleus. Emission intensity was three times greater for L_2P_4 than L_2P_3 in the EBV-positive C666-1 cells.

Selective toxicity of L_2P_4 towards EBV-positive cells.

EBNA1 can only facilitate DNA replication of EBV by forming homodimers; therefore, blocking dimer formation provides a route by which to kill EBV-infected tumour cells. As is well known, the EBNA1 dimer is formed through the YFMVF-mediated interface, and this can be examined via an 3-maleimidobenzoyl N-hydroxysuccinimide ester (MBS) cross-linked dimerization assay; MBS is an amine- to-sulfhydryl crosslinker. The MBS-mediated protein crosslink- ing effect was represented as the dimer to monomer ratio. The importance of YFMVF for dimerization was further investigated in the WT-EBNA1 and EBNA1 mutants (EBNA1-Y561A, EBNA1- M563A, EBNA1F565A and EBNA1-3A) via its homodimerization efficiency. The results showed that the dimerization efficiency was greatly decreased for EBNA1-3A, while a relatively small decrease in the efficiency was observed for the other three point mutants (Supplementary Fig. 27). Consistent with this observation and the luminescence titration experiment, the MBS cross-linked dimerization assay was also clearly inhibited by the designed probes, as shown in Fig. 4a–d ($P < 0.001$).

Considering the strong binding of L2P4 to WT-EBNA1 and the selective in vitro nuclear imaging, we investigated whether L2P4 exhibited selective and efficient cytotoxicity towards EBV-positive cells. An MTT (3-(4,5-dimethylthiazol-2-yl)-2,5-diphenyltetrazo- lium bromide) cytotoxicity assay was carried out for the three pep- tides (P2, P3 and P4; Supplementary Fig. 31) and the three peptide conjugates (L2P2, L2P3 and L2P4; Fig. 4e–j) in three EBV-negative cell lines (MRC-5 (normal lung fibroblasts), HeLa and Ramos) and three EBV-positive cell lines (C666-1, NPC43 and Raji). All probes (conjugates) were found to exhibit weak cytotoxicity in EBV- negative cells even at high doses (50 μM), and they all showed dose- dependent cytotoxicity in EBV-positive cells. L2P4 was the most cytotoxic in all three EBV-positive cells. It is noteworthy that the order of probe cytotoxicity in EBV-positive cells (L2P4 > L2P3 > L2P2) was the same as that for the MD simulation, luminescence titration and in vitro imaging results.

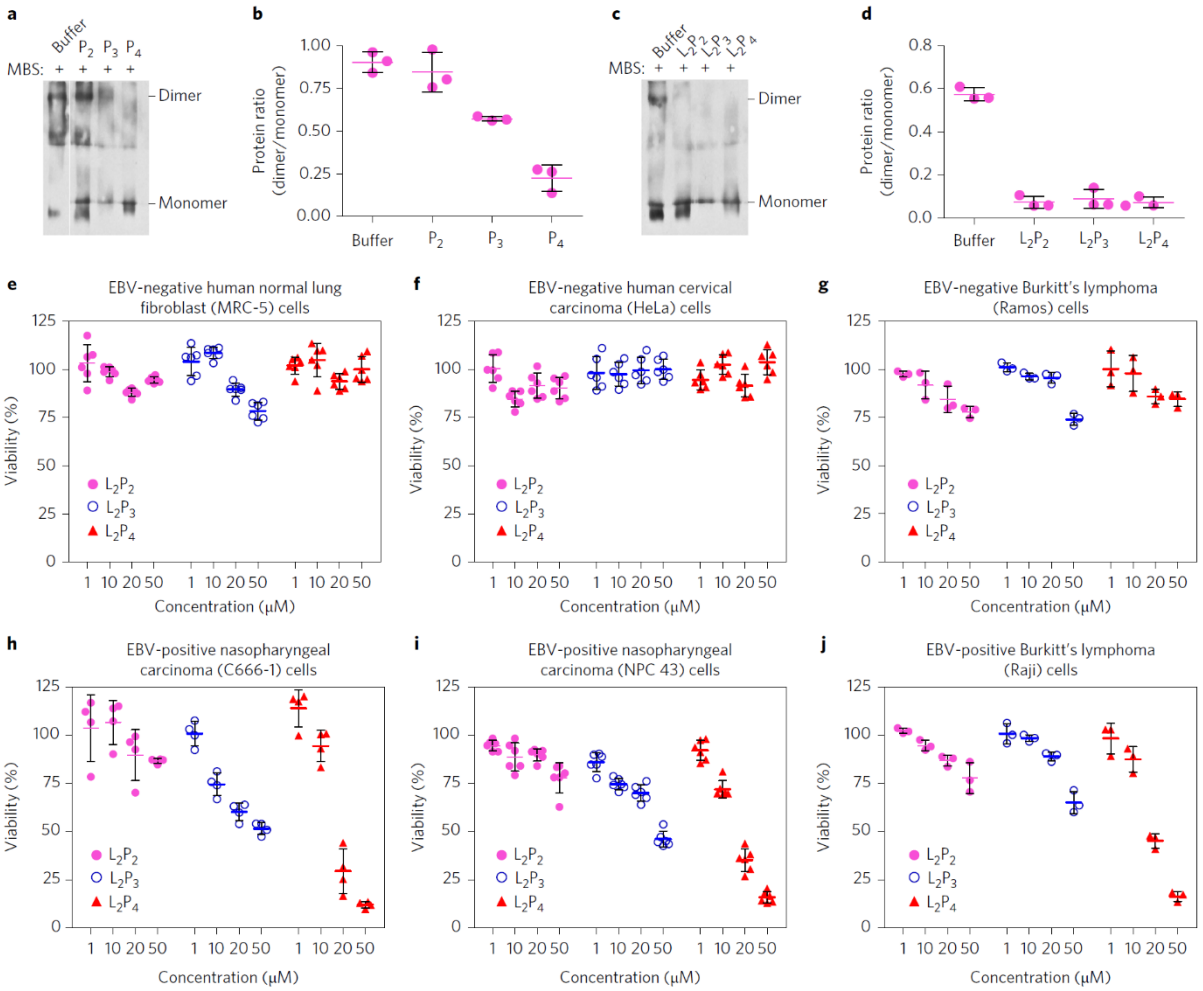

Figure 4 | Homodimerization and cytotoxicity assays. **a**–**d**, WT-EBNA1 was subjected to MBS cross-linked dimerization assays after addition of peptides (P_2–P_4, **a** and **b**) and peptide conjugates (L_2P_2–L_2P_4, **c** and **d**). The inhibitory efficiency was measured as the EBNA1 dimer/monomer ratio (**b** and **d**); the intensity of each protein band represents the mean ± s.d. of three independent experiments. **e**–**j**, Cytotoxicity (MTT assay) of the conjugate probes to EBV-negative (e–g) and EBV-positive (**h**–**j**) cells lines after 24 h. Each measurement was performed in triplicate, and repeated twice. The data represent the mean ± s.d.

In vivo tumour imaging and inhibition of L2P4.

To further evaluate the *in vivo* performance of L_2P_4, intra-tumoural injections of P_4 or L_2P_4 (low dose (L) of 2 μg or high dose (H) of 4 μg) were administered to C666-1 and HeLa cell xenografts in BALB/c nude mice. The injections were carried out biweekly along with body weight and tumour measurements. Mice carrying HeLa cell xenografts served as controls to confirm the specificity of the *in vivo* targeting effect of P_4 or L_2P_4. Treatment with P_4 or L_2P_4 had no significant effects on the body or organ weights of the mice when compared with controls (Supplementary Figs 32, 33 and 35a), indicating that neither P_4 nor L_2P_4 exhibited a toxic effect *in vivo*. C666-1 cell xenograft growth was effectively inhibited, whereas the growth of HeLa cell xenografts was unaffected by treatment with P_4 or L_2P_4 (Fig. 5d and Supplementary Fig. 35b). By day 7, treatment of C666-1 cell xenografts with P_4-L, P_4-H and L_2P_4-H had significantly decreased the tumour volumes versus controls, and at the end of the experiment (day 21), the average tumour volumes were decreased by 65.7%, 65.5% and 92.3% ($P<0.05$, $P<0.005$ and $P<0.001$), respectively (Fig. 5d and Supplementary Fig. 34). For the HeLa cell xenografts, there were no significant differences in average tumour volume between control mice and those treated with P4 or L2P4 (low and high dose) at the end of the experiment (day 18), as shown in Supplementary Fig. 35b. At the end of the experiment, the mice were killed and the tumours were excised and weighed. For C666-1 cell xenografts, average tumour weights were decreased after treatment with P_4-L, P_4-H and L_2P_4-H by 72.6%, 86.6% and 92.8% (not significant, $P < 0.05$ and $P < 0.005$), respectively, when compared with controls (Fig. 5a–c,e). Whereas for the HeLa cell xenografts, there were no significant differences in the average tumour weights (Supplementary Figs 35c and 36). The significant and selective inhibition of EBV-positive tumour growth by P_4 and L_2P_4 confirmed their EBV-targeting specificity and indicated that the conjugation of L_2 to P_4 does not affect it tumour inhibitory effect.

Fluorescence imaging of the excised C666-1 tumours showed that the L2P4 fluorescence signal was detectable 48 h after the intra-tumoural injection (Fig. 5f). As expected, no fluorescent sig- nal was detected in control or P4 treated tumours.

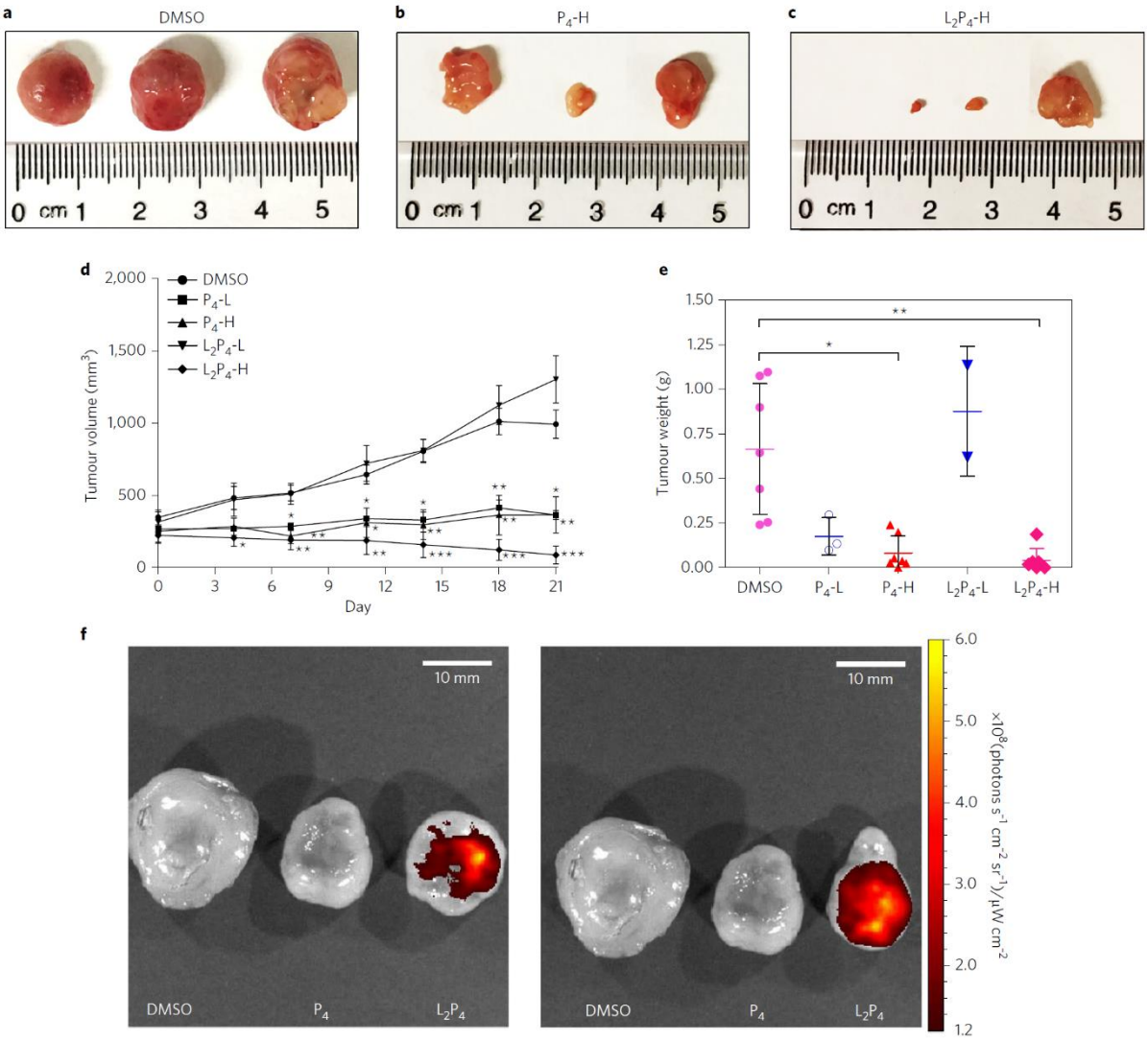

Figure 5 | *In vivo* studies of P_4 and L_2P_4 as EBV-specific anti-cancer agents. a–e, *In vivo* tumour inhibition assays for P_4 and L_2P_4. Mice were given intra-tumoural injections of P_4, L_2P_4 or dimethylsulfoxide (DMSO; vehicle and control) twice-weekly for 21 days; high (H) and low (L) doses were 4 and 2 μg per tumour, respectively. At the experimental endpoint, the tumours were excised and photographed (a–c), and their volumes (**d**) and weights (**e**) were measured; for grouping and measurement numbers, see Supplementary Table 6. Data are expressed as the mean ± SEM. $*P < 0.05$; $**P < 0.005$. , Representative fluorescence images of excised C666-1 tumours. Tumours were excised directly after the mice were killed and the fluorescence intensity was measured using an IVIS Lumina system (excitation, 460 nm; emission, 520 nm) 48 h post intra-tumoural injection. Fluorescence was quantified as the total radiant efficiency, (photons s^{-1} cm^{-2} sr^{-1})/μW cm^{-2}. Image: min = 0.00, max = 5.59 × 10^8 (photons s^{-1} cm^{-2} sr^{-1}/μW cm^{-2}).

Discussion

Our initial MD studies suggested that a network of hydrophobic interactions and salt bridging mediates the binding of L_2P_4 to the dimeric interface of EBNA1 (Fig. 1). The selective and strong bind- ing of L_2P_4 to EBNA1 was further confirmed using luminescence titration experiments (Fig. 2). L_2P_4 was found to localize in the nuclei of EBV-positive cells, but not in those of EBV-negative cells. The selective emission of L_2P_4 in the nucleus was generated by its binding with EBNA1 (Fig. 3).

Our study also revealed that EBNA1 mutants (especially EBNA1- 3A) were not able to undergo homodimerization (Supplementary Fig. 27), emphasizing the importance of the dimeric interface (YFMVF) to EBNA1 dimer formation. The analysis of the WT- EBNA1 dimerization efficiency on addition of the designed probes using an MBS cross-linked dimerization assay showed that the probes can significantly interfere with EBNA1 dimer formation (Fig. 4a – d). Extensive cytotoxicity assays performed on both EBV- positive and-negative cells demonstrated the significant and selective inhibition of EBV-positive cell growth by L_2P_4, and more importantly, revealed that the reason for the selective cytotoxicity is the inhibition of the EBNA1 dimerization process (Fig. 4e – j). Finally, experiments investigating the effects of L_2P_4 on mice carrying C666-1 and HeLa cell xenografts confirmed that it specifically targets EBV, and they showed that our rationally designed probe can be applied *in vivo* to target and inhibit the growth of EBV-positive tumours (Fig. 5).

Our data clearly demonstrates that L_2P_4 can selectively inhibit EBV-positive tumours—*in vitro* and *in vivo*—and that it achieves this by interfering with EBNA1 homodimerization. We are confident that this work will revive research interest and open new doors in the study of EBNA1 inhibition by shining light on previously unknown areas—visualization of the probe’ s binding to EBNA1 and the dimerization inhibition process in the nucleus of EBV-positive cells. L_2P_4 is a solid foundation for future research into areas such as therapeutic agents for EBV-related malignancies and probes for imaging the zinc- finger region of EBNA1 homodimers.

Methods

Molecular dynamics simulation.

All the simulations reported herein were performed using the unbiased MD program in the Amber 14 software package. The ff99SBildn force field[23] has been used to describe all molecular systems. For each of the simulations, the peptide was solvated in a periodic truncated cubic box with TIPC[24] water molecules, providing a 10 Å buffer distance between the peptide surface and the periodic box edge. The peptide was then heated from 100 K to 300 K in 20 ps. The system was further equilibrated for 200 ps with constant pressure and temperature (NPT) before starting the 200 ns NPT production simulation. A 2 fs time step and the SHAKE-enabled setting were used during the equilibration and production stages, and a Berendsen thermostat was used for temperature control. Detailed MD simulations of peptides/probe–EBNA1 complexes can be found in the Supplementary Materials.

Luminescence titration analysis.

The binding constants and selectivity of the probes were measured by luminescence titration analysis. This was conducted via the gradual addition of various analytes (for example, WT-EBNA1, EBNA1 mutants, BSA and metal ions), which was then stopped, either when the volume of added analyte equalled 5% of the probe volume or the influence on luminescence was saturated.

Preparation of protein samples.

Five protein samples were used during this work. WT-EBNA1 protein (379 – 641 residues) fused with glutathione S-transferase was expressed in Escherichia coli and purified using glutathione sepharose 4B rinse (GE Dharmacon). Then 5 μ g of EBNA1 was prepared and incubated with MBS at 37 ˚C for 10 min. The protein was separated on an SDS-PAGE gel, transferred onto a nitrocellulose membrane and blotted with antibodies (#RG001040, Solarbio, Bioscience and Technology). EBNA1 mutant proteins were prepared by mutation of YFMVF to FFAVA (yielding the EBNA1-3A mutant) or by conservative point mutation of Y_{561}, M_{563} and F_{565} to A (yielding EBNA1-Y_{561}A, EBNA1-M_{563}A and EBNA1-F_{565}A) through site-directed mutagenesis.

Cell culture.

The EBV-negative MRC-5 and HeLa cells were provided by the Shanghai cell bank, Chinese Academy of sciences; the EBV-negative CNE2 and EBV-positive C666-1 cells were supplied by the Hong Kong NPC AoE Cell Line Repository; the EBV-negative Burkitt's lymphoma Ramos and EBV-positive Burkitt's lymphoma Raji cells were provided by H. L. Lung; the NPC43 cells were contributed by S. W. Tsao.

MRC-5 cells were grown in MEM medium; HeLa (cervical carcinoma) cells were grown in DMEM; CNE2, C666-1, Ramos and Raji cells were grown in RPMI 1640 medium. All medium used was supplemented with 10% serum (FBS), 1% penicillin and streptomycin at 37 °C and 5% CO2. NPC43 cells were maintained in RPMI 1640 with 10% FBS and 4μM Y27632 (inhibitor of Rho-associated, coiled-coil-containing protein kinase; Enzo Life Sciences).

NPC43 cells were established from the surgically resected NPC tissue of a 64-year-old male patient, with stage III recurrent NPC. The cells harbour the EBV virus and were kept in RPMI supplemented with 10% FBS and 4 μM Y27632 over the course of 200 population doublings. NPC43 cells are tumourigenic when injected (ten million cells) at a subcutaneous site in NOD/SCID mice. Short tandem repeats profiling confirmed the NPC patient as the origin of the cells. The NPC43 cells were induced to undergo lytic reactivation of EBV by treatment with 12-O-etradecanoylphorbol-13-acetate/sodium butyrate. Infectious EBVs were harvested from the supernatant of NPC43 cells. All cell lines used in this study were tested and confirmed to be mycoplasma-negative, and authenticated by using the AmpFLSTR Identifier PCR amplification kit (Life Technologies).

Flow cytometry analysis.

HeLa and C666-1 cells (105 per sample) were seeded onto 35 mm Petri dishes overnight. Afterwards, the cells were incubated with the probes as indicated, and then washed with PBS several times. Cellular uptake was evaluated by flow cytometry under 488 nm excitation generated by an argon laser. The emission was obtained using FL2-H (log). One thousand events were analysed to get the cellular uptake.

In vitro imaging and co-staining.

Cells were incubated with L2P2, L2P3 or L2P4 (10 μM) for 6 h, and then co-stained with LysoTracker Green DND-26 (Thermo Fisher), MitoTracker Green FM (M7514, Thermo Fisher) and Hoechst 33342 nuclear dye for 1 h (all at 1 nM). Imaging was conducted using a multi-photon Leica SP8 confocal microscope, equipped with a coherent femtosecond laser (680 – 1,050 nm), argon laser (432 nm, 457 nm and 488 nm), He – Ne laser (632 nm), ultraviolet lamp and a controlled CO2-content stage-top tissue culture chamber (2 – 7% CO2, 37 ˚C).

Cytotoxicity tests.

The MTT viability assay was performed according to standard methods. In brief, cells (3 × 103 per well) were seeded onto 96-well plates 24 h before exposure to the probes. The cells were incubated with the probes in the dark for another 24 h. The cytotoxicity was determined by the MTT reduction assay. The cell monolayers were rinsed with PBS and then incubated with 50 μl of MTT solution (0.5 mg ml−1) at 37 ˚C for 3 h. Then solution was then removed, and 100 μl of dimethylsulfoxide solubilizing reagent was added before shaking for 30 min to dissolve the formazan crystals produced in the living cells. The absorbance of the formazan crystals was measured at 540 nm and 690 nm, using a dual-wavelength Labsystem Multiskan microplate reader (Merck Eurolab).

Nude mice carrying C666-1 or HeLa xenografts.

C666-1 or HeLa cells were suspended at 1 × 107 in 150 µl of serum-free medium (C666-1) or serum-free medium mixed 1:1 with Matrigel (BD Biosciences) (HeLa), and injected into the right flanks of male (C666-1) or female (HeLa) six- to eight-week-old BALB/c nude mice, which were obtained from BioLASCO. When tumours reached an average volume of 200–300 mm3, but before initiation of treatment, the xenografted mice were assigned to groups (for grouping refer to Supplementary Tables 6 and 7) based on tumour volume (within each group tumour volume did not vary by more than 10%). An analysis of variance was performed to ensure that there were no statistical differences between the groups. P4 and L2P4 in 0.1% dimethylsulfoxide at the desired dose (2 or 4 µg per tumour; low or high dose) were injected directly into the tumour using a 29 gauge syringe. Mice receiving an equivalent volume of 0.1% dimethylsulfoxide alone served as controls. Body weight and tumour volumes were measured twice weekly. Tumour volumes were calculated as (length × width2)/2. Intra-tumoural tumour injections were repeated twice weekly, after which the mice were killed and their tumours harvested and weighed. Investigators were blind to the treatment groups during the experiments and data analysis. All animals were included in the analysis. No power analyses were used to calculate the sample size for the animal studies. All animal experiments were approved by the Department of Health of the Hong Kong Government, Hong Kong Baptist University Committee on the Use of Human and Animal Subjects in Teaching and Research and the Animal Subjects Ethics Sub-Committee of Hong Kong Polytechnic University.

Statistical analysis.

The intensity of the protein bands and raw images were measured using Gel-Pro Analyzer v.4.0 (Media Cybernetics) to obtain the average of three independent experiments (mean ±s.d.). The results were presented as a column plot in GraphPad Prism 5.0. Single factor analysis of variance was used to detect the significance of differences. For the MTT assay, each dose concentration was performed in triplicate wells, and repeated twice. Data are expressed as the mean ±s.d. Statistical analyses of tumour size and volume in the animal studies were conducted using the Student's *t*-test. Results of $P < 0.05$ are considered significant. Data are expressed as the mean ± s.d.

Data availability.

The authors declare that all data supporting the findings of this study are available in the paper and its Supplementary Information. In addition, underlying research data for this paper is available in accordance with the Engineering and Physical Science Research Council (EPSRC) open data policy from http//:dx.doi.org/10.15128/r2v692t620b.

Acknowledgements

This work is funded by the Hong Kong Baptist University (FRG2/14-15/013013), Hong Kong Polytechnic University (HKPolyU), Hong Kong Research Grants Council (HKBU 20301615), Hong Kong Polytechnic University Central Research Grant (G-UC08), Hong Kong Research Grants Council (PolyU 153012/15P), University Research Facility for Chemical and Environmental Analysis (UCEA) and Area of Excellent Grants (1-ZVGG) of Hong Kong Polytechnic University, ECS-Grant - RGC (PolyU 253002/14P), HK PolyU (PolyU 5096/13P), HKBU and HKPolyU Joint Research Programme (RC-ICRS/15-16/02F-WKL02F-WKL), the EPSRC (Durham University, DTA award) and Research Grants Council of the Hong Kong SAR for the NPC Area of Excellence (AoE/M 06/08 Center for Nasopharyngeal Carcinoma Research).

Author contributions

N.-K.M. and K.-L.W. conceived and supervised the project. L.J. performed the synthesis, characterization, spectroscopic properties measurements and cytotoxicity assays in normal and some EBV-negative cells; H.L. contributed the photophysical data analysis. R.L. purified the WT-EBNA1 and EBNA1 mutants, and conducted the dimerization assay; T.H., Z.-X.B. and W.-T.W. contributed to the MD simulations; C.-F.C. carried out the confocal imaging, co-localization and some cytotoxicity assays; S.L., J.Z. and S.L.C. performed the peptide synthesis and purified the peptide conjugates; W.-Y.W., M.M.- L.L., B.D.C. and W.C.S.T. carried out the in vivo inhibition. M.L.L., H.L.L., S.W.T. and G.S.T. contributed to the in vitro cytotoxicity in EBV-positive and EBV-negative pairs of cancer cell lines; G.-L.L. participated in the cell work and molecular design; L.J., W.-L.C., W.-S.L., G.-L.L., S.L.C. and K.-L.W. wrote the manuscript.

Competing interests

The authors declare no competing financial interests.

References

1. Cohen, J. I. Epstein – Barr virus infection. *N. Eng. J. Med.* **343,** 481 – 492 (2000).
2. Young, L. S. & Rickinson, A. B. Epstein – Barr virus: 40 years on. *Nat. Rev. Cancer* **4,** 757 – 768 (2004).
3. Thorley-Lawson, D. A. Epstein – Barr virus: exploiting the immune system. *Nat. Rev. Immunol.* **1,** 75–82 (2001).
4. Paludan, S. R., Bowie A. G., Horan K. A. & Fitzgerald K. A. Recognition of herpesviruses by the innate immune system. *Nat. Rev. Immunol.* **11,** 143 – 154 (2011).
5. Wood, V. H. J. *et al.* Epstein – Barr virus-encoded EBNA1 regulates cellular gene transcription and modulates the STAT1 and TGFb signalling pathways. *Oncogene* **26,** 4135 – 4147 (2007).
6. Frappier, L. The Epstein – Barr virus EBNA1 protein. *Scientifica* **2012,** 438204 (2012).
7. Li, N., Thompson, S., Jiang, H., Liberman, P. M. & Luo, C. Development of drugs for Epstein – Barr virus using high-throughput *in silico* virtual screening. *Expert Opin. Drug Discov.* **5,** 1189 – 1203 (2010).
8. Kim, S. Y. *et al.* Small molecule and peptide-mediate inhibition of Epstein – Barr virus nuclear antigen 1 dimerization. *Biochem. Biophys. Res. Commun.* **424,** 251 – 256 (2012).
9. Jiang, L. *et al.* EBNA1-specific luminescent small molecules for the imaging and inhibition of latent EBV-infected tumor cells. *Chem. Commun.* **50,** 6517 – 6519 (2014).
10. Fisher, N., Vo, M. D., Mueller-Lantzsch, N. & Grässer, F. A. A potential NES of the Epstein – Barr virus nuclear antigen 1 (EBNA1) does not confer shuttling. *FEBS Lett.* **447,** 311 – 314 (1999).
11. Kanda, T., Otter, M. & Wahl, G. M. Coupling of mitotic chromosome tethering and replication competence in Epstein – Barr virus-based plasmids. *Mol. Cell. Biol.* **21,** 3576 – 3588 (2001).
12. Vacik, J., Dean, B. S., Zimmer, W. E. & Dean, D. A. Cell-specific nuclear import of plasmid DNA. *Gene Ther.* **6,** 1006 – 1014 (1999).
13. Bochkarev, A., Bochkareva, E., Frappier, L. & Edwards, A. M. The 2.2 Å structure of a permanganate-sensitive DNA site bound by the Epstein–Barr virus origin binding protein, EBNA1. *J. Mol. Biol.* **284,** 1273–1278 (1998).
14. Correia, B. *et al.* Crystal structure of the gamma-2 herpesvirus LANA DNA binding domain identifies charged surface residues which impact viral latency. *PLoS Pathog.* **9,** e1003673 (2013).
15. Case, D. A. *et al.* Amber 14 (Univ. California, San Francisco, 2014).
16. Lippert, E. *et al. Umwandlung von elektronenanregungsenergie. Angew. Chem.* **73,** 695 – 706 (1961).
17. Grabowski, Z. R. & Rotkiewicz, K. Structural changes accompanying intramolecular electron transfer: focus on twisted intramolecular charge-transfer states and structures. *Chem. Rev.* **103,** 3899–4031(2003).
18. Sahoo, D. & Chakravorti, S. Dye-surfactant interaction: modulation of photophysics of an ionic styryl dye. *Photochem. Photobiol.* **85,** 1103 – 1109 (2009).
19. Wandelt, B., Mielniczak, A., Turkewitsch, P., Darling, G. D. & Stranix, B. R. Substituted 4-[4-(dimethylamino)styryl] pyridinium salt as a fluorescent probe for cell microviscosity. *Biosens. Bioelectron.* **18,** 465 – 471 (2003).
20. Chakraborty, A., Kar, S. & Guchhait, N. Secondary amino group as charge donor for the excited state intramolecular charge transfer reaction in trans-3-(4-monomethylamino-phenyl)-acrylic acid: spectroscopic measurement and theoretical calculations. *J. Photochem. Photobiol. A* **181,** 246–256 (2006).
21. Mahon, K. P. *et al.* Deconvolution of the cellular oxidative stress response with organelle-specific peptide conjugates. *Chem. Biol.* **14,** 923 – 930 (2007).

22. Puckett, C. A. & Barton, J. K. Targeting a ruthenium complex to the nucleus with short peptides. *Bioorg. Med. Chem.* **18,** 3564 – 3569 (2010).

23. Lindorff-Larsen, K. et al. Improved side-chain torsion potentials for the amber ff99SB protein. *Proteins* **78**, 1950 – 1958 (2010).

24. Jorgensen, W. L., Chandrasekhar, J., Madura, J. D., Impey, R. W. & Klein, M. L. Comparison of simple potential functions for simulating liquid water. *J. Chem. Phys.* **79**, 926 – 935 (1983)